Fracture evaluation of ultra-high-performance fiber reinforced concrete (UHPFRC)

Zhang, Youyou; Xin, Haohui; Correia, José A.F.O.

DOI
10.1016/j.engfailanal.2020.105076

Publication date
2021

Document Version
Final published version

Published in
Engineering Failure Analysis

Engineering Failure Analysis 120 (2021) 105076

Contents lists available at ScienceDirect

Engineering Failure Analysis

journal homepage: www.elsevier.com/locate/engfailanal

Fracture evaluation of ultra-high-performance fiber reinforced concrete (UHPFRC)

Youyou Zhang [a], Haohui Xin [a,b,*], José A.F.O. Correia [c]

[a] Department of Civil Engineering, School of Human Settlements and Civil Engineering, Xi'an Jiaotong University, Xi'an, China
[b] Civil Engineering and Geosciences, Delft University and Technology, Netherlands
[c] INEGI & CONSTRUCT, Faculty of Engineering, University of Porto, Portugal

ARTICLE INFO

Keywords:
Ultra-high-performance concrete (UHPC)
Ultra-high-performance fiber-reinforced concretes (UHPFRC)
Engineering tensile and compressive stress-strain relationships
Mixed mode crack propagation

ABSTRACT

The development of numerical simulation for Ultra-high-performance concrete (UHPC) and Ultra-high-performance fiber-reinforced concretes (UHPFRC) is fundamental for the design and construction of related structures. The simplified engineering stress-strain relationship and the input values are necessary in the finite element modeling. Four-linear curves and modified Kent–Park model were proposed to describe the engineering tensile and compressive stress-strain relationship, respectively. An attempt was made to simulate the fracture of UHPC and UHPFRC using concrete damaged plasticity model and element deletion strategies. The predicted tensile and compressive behaviors of UHPC and UHPFRC were successfully validated by the test results in the literature. For a better understanding of the mechanical behavior of UHPC and UHPFRC exposed to biaxial loadings, mixed-mode crack propagation simulation on the double-notched specimens exposed to combined shear-tensile and shear-compressive forces was discussed.

1. Introduction

The ultra-high-performance concrete (UHPC) and ultra-high performance fiber reinforced concrete (UHPFRC) are cementitious material with favorable material properties, including high strength (compressive strength > 150 MPa and tensile strength > 8 MPa [1]) and strain-hardening under uniaxial loading[2]. The above outstanding performance is credit to the dense microstructures of UHPC/UHPFRC[3]. With improved high strength and durability properties[4–8], UHPC/UHPFRC is suitable for new structures exposed to heavy loads, such as I-shaped beams[9], bridges deck[8], piers[10], in the field of highway transportation infrastructure [11] and in the replacement of aging concrete structures or components[12–16]. The UHPC/UHPFRC is also promising to be an alternative of normal concrete in steel/FRP-concrete composite structures to improve its mechanical performance, such as beams [17,18], composite column[19], composite joints[20–22], shear connectors[23–25], and GFRP-concrete bridge deck[26–28].

Recently, several studies have been reported related to the mechanical properties and numerical simulation of UHPC/UHPFRC. Shafieifar et al. [3] experimentally determined the compressive ultimate capacity of UHPC through the cylinder and cube compressive test, and tensile ultimate capacity using flexural, briquette, and splitting tension tests, respectively. The results showed that the compressive strength of commercial UHPC was three to four times greater than normal strength concrete, the tensile strength and ductility of UHPC was two to four times greater than normal strength concrete. Graybeal et al. [9] investigated the flexural behavior of a prestressed I-shaped UHPC girder. The cracking, flexural stiffness, and moment capacity are discussed and compared to predictions

* Corresponding author.
E-mail address: h.xin@tudelft.nl (H. Xin).

https://doi.org/10.1016/j.engfailanal.2020.105076
Received 20 June 2020; Received in revised form 17 September 2020; Accepted 4 November 2020
Available online 9 November 2020

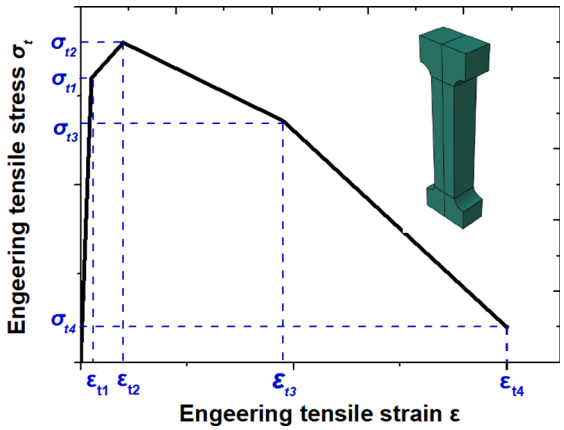

Fig. 1. Simplified engineering tensile stress-strain relationship of UHPC and UHPFRC.

Table 1
Parameters of simplified engineering tensile stress-strain relationship of UHPC and UHPFRC (Unit: με for strain, MPa for stress).

		ϵ_{t1}	σ_{t1}	ϵ_{t2}	σ_{t2}	ϵ_{t3}	σ_{t3}	ϵ_{t4}	σ_{t4}
UHPC	7d	102.1	3.67	151.0	4.42	208.0	3.13	278.0	0.0
	14d	123.2	3.56	208.8	4.95	269.0	3.70	346.3	0.0
	28d	135.1	4.76	174.3	5.29	189.5	4.09	200.7	0.0
UHPCFRC	7d	185.0	7.93	3200.0	9.02	19720.9	6.85	33020.6	0.76
	14d	177.0	7.57	2300.0	8.91	33120.0	4.11	43980.7	0.67
	28d	196.0	8.40	4190.0	9.13	31300.9	6.87	50620.9	1.28

from the AASHTO standard. Soetens & Matthys [29], and López et al. [30] investigated the cracking strength and the post-cracking strength of UHPFRC using empirical formulations and cohesive models, respectively. Yoo et al.[30] investigated the effects of steel fibers types (short, medium-length, and long) on the flexural behaviors of UHPFRC. Rios et al. [31] experimentally investigated the tensile properties of UHPFRC manufactured with short and long fibers. The results showed that the type of fibers will affect the porosity distribution, and the tensile properties. Wang et al. [10] employed the modified Kent–Park model to describe the compressive stress-strain relationship of UHPFRC and evaluated the seismic performance of bridge pier made of UHPFRC. Mao et al. [31] simulated the performance of UHPFRC subjected to blast loading, the performance of the numerical models were verified by comparing modeling results to the data from corresponding full-scale blast tests. Li et al. [32] conducted a series of tests to investigate the performance of the UHPC slab exposed to explosive loading. Numerical simulation was conducted, and the feasibility and validity of the numerical predictions of UHPC slab responses were validated by test results.

The development of numerical simulation is fundamental for the design and construction of structures made of UHPC/UHPFRC. The simplified engineering stress-strain relationship and the input values in the finite element models are necessary for UHPC/UHPFRC applications in the civil engineering structures. However, the literature related to simplified engineering stress-strain relationship and the simulation of UHPC/UHPFRC was not sufficient as far as the authors' knowledge. It is also noted that the UHPC fracture is modelled based on the average value of the test results, and the combination of UHPC fracture simulaton with probabilistic analysis [33–35] is an very interesting topic, which will be further investigated in the future.

In this paper, an attempt was made to simulate the fracture of UHPC/UHPFRC using concrete damaged plasticity model and element deletion strategies. The simplified model was proposed to describe the engineering stress-strain relationship. The input values to simulate the fracture of UHPC and UHPFRC based on the commercial finite element software [36] were discussed. The simulation results were validated by the test results in the literature. The crack propagation under combined axial (tensile and compressive)-shear forces was investigated based on the validated material model.

2. Simplified Engineering Stress-Strain Relationship

The simplified model of engineering stress-strain relationship for UHPC and UHPFRC is discussed in this section based on the test results reported in the literature[2]. The mixed constitution of UHPC is listed as below[2]: 657 kg/m^3 cement, 418 kg/m^3 Ground Granulated Blast Furnace Slag (GGBS), 119 kg/m^3 silica fume, 1051 kg/m^3 silica sand with a average size of 0.27 mm, 40 kg/m^3 superplasticizers, and 185 kg/m^3 water. Compared with UHPC, steel fibers with the volume ratio of 2% (157 kg/m^3) were added for the UHPFRC. The length and diameter of steel fibers were 13 mm and 0.2 mm, respectively. The tensile behavior of UHPC and UHPFRC was obtained by a direct tensile test using dog-bone specimens with a size of the cross-section of 26 mm by 50 mm, and the compressive behavior of UHPC and UHPFRC was obtained by uniaxial compression tests using a cylinder specimens with a diameter of 50 mm and a length of 100 mm[2].

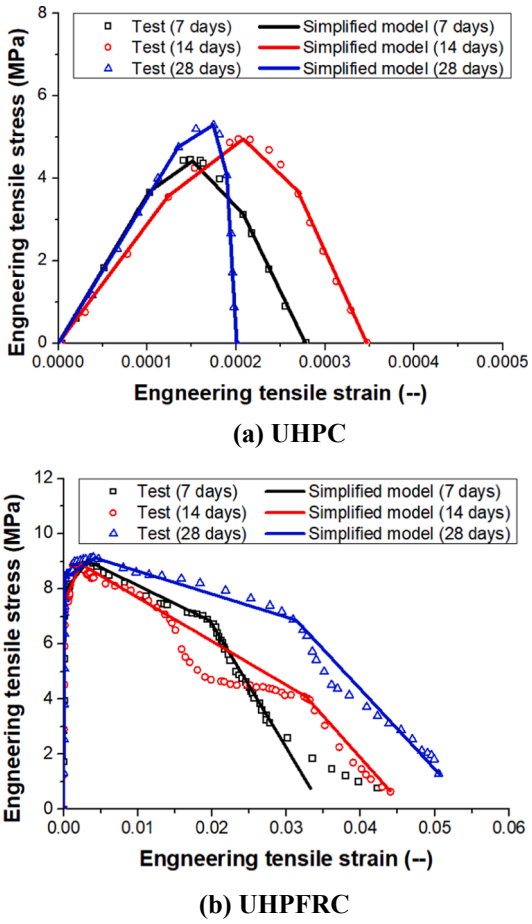

Fig. 2. Engineering tensile stress-strain comparison.

2.1. Tensile behaviors

To describe the engineering tensile stress-strain relationship of UHPC/UHPFRC with both accuracy and simplicity, a model with four-linear curves was proposed in this paper, as shown in Fig. 1. The point $(\varepsilon_{t1}, \sigma_{t1})$ is the corresponding strain and stress at end of the linear curve, $(\varepsilon_{t2}, \sigma_{t2})$ is the corresponding strain and stress when the tensile stress reaches the peak; $(\varepsilon_{t3}, \sigma_{t3})$ is the corresponding strain and stress at the stiffness turning point in the softening stage; and $(\varepsilon_{t4}, \sigma_{t4})$ is the corresponding strain and stress at the rupture. The parameters of simplified engineering tensile stress-strain of UHPC and UHPFRC at 7, 14, and 28 days after casting are calibrated in Table 1. The comparisons between the simplified model and experimental results in [2] are shown in Fig. 2. A good agreement is observed, indicating that the simple four-linear curves could successfully describe the engineering tensile stress-strain relationship of UHPC/UHPFRC.

The ductility of UHPFRC is higher than UHPC based on Fig. 2. The ratio σ_{t1}/σ_{t2} is 0.83, 0.72 and 0.90 for UHPC at 7, 14 and 28 days, and is 0.88, 0.85 and 0.92 for UHPFRC at 7, 14 and 28 days, respectively. The ratio σ_{t3}/σ_{t2} is 0.71, 0.75 and 0.77 for UHPC at 7, 14 and 28 days, and is 0.75, 0.46 and 0.75 for UHPFRC at 7, 14 and 28 days, respectively. The ratio σ_{t4}/σ_{t2} is zero for UHPC and is 0.08, 0.08, and 0.14 for UHPFRC at 7, 14, and 28 days respectively. The difference in stress ratio between UHPFRC and UHPC is relatively smaller than the strain ratio.

2.2. Compressive behaviors

The modified Kent-Park model [37,38] was proposed to describe the engineering compressive stress-strain relationship of UHPC and UHPFRC as shown in Eq. (1).

Table 2
Parameters to determine engineering compressive stress-strain relationship of UHPC and UHPFRC (Unit: με for strain, MPa for stress and modulus).

Items	UHPC			UHPFRC		
	7 days	14 days	28 days	7 days	14 days	28 days
σ_{pk}	146.0	149.1	150.6	124.3	124.1	121.3
ε_0	3651	4168	3730	3260	3284	3238
λ_{rs}	0.38	0.35	0.38	0	0	0
ε_{20}	3826	4341	3947	4000	5000	4000
E_c	45,370	44,830	45,550	41,140	42,090	42,080

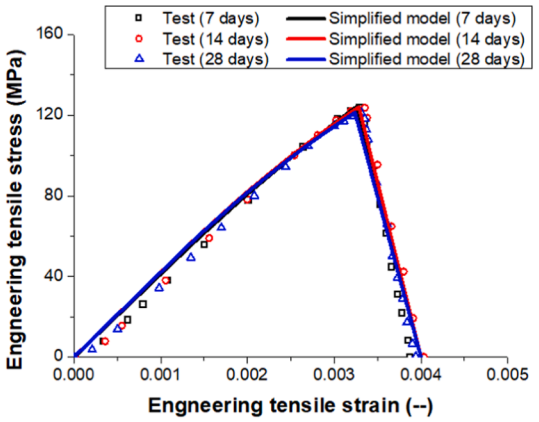

(a)UHPC

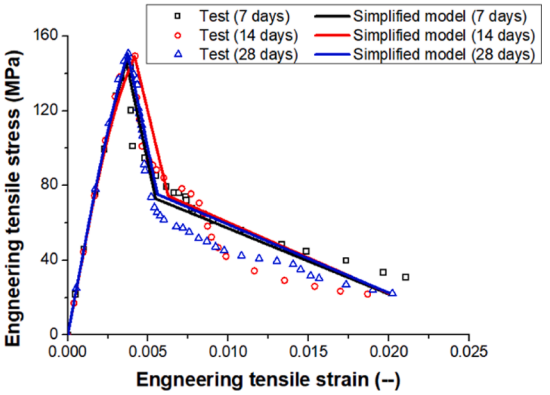

(b) UHPCFRC

Fig. 3. Engineering compressive stress-strain comparison.

$$\sigma_c = \begin{cases} \sigma_{pk}\left[2\varepsilon_c/\varepsilon_0 - (\varepsilon_c/\varepsilon_0)^2\right] & \varepsilon_c \leqslant \varepsilon_0 \\ \sigma_{pk}\left[1 - \dfrac{(1-\lambda_{rs})(\varepsilon_c - \varepsilon_0)}{(\varepsilon_{20} - \varepsilon_0)}\right] & \varepsilon_0 < \varepsilon_c \leqslant \varepsilon_{20} \\ \lambda_{rs}\sigma_{pk} & \varepsilon_c > \varepsilon_{20} \end{cases} \tag{1}$$

Where: ε_c and σ_c are the compressive strain and stress of the concrete, respectively; σ_{pk} and ε_0 are the peak compressive stress and the corresponding strain of the concrete, respectively; λ_{rs} is the ratio of the residual strength to the peak stress; ε_{20} is the beginning strain point of the residual strength $\lambda_{rs}\sigma_{pk}$. The ε_{20} could be determined based on the following equation:

$$\varepsilon_{20} = \frac{(0.65 - \lambda_{rs})\sigma_{pk}}{0.0103} + \frac{0.65\sigma_{pk}}{E_c} \tag{2}$$

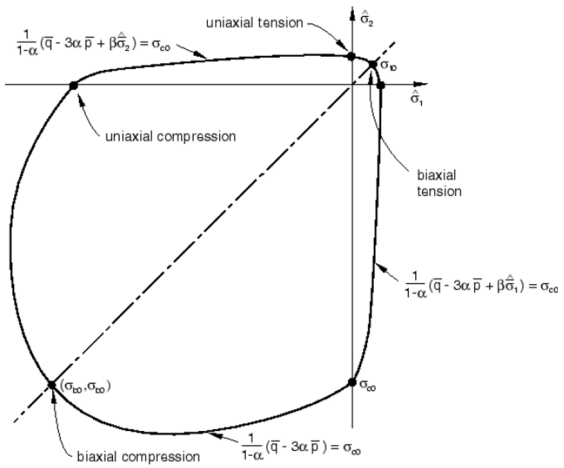

Fig. 4. Yield surface of CDP model in-plane stress [36].

For UHPC/UHPFRC, the engineering compressive stress and strain relationship could be determined by Eq. (1) when four parameters σ_{pk}, ε_0, λ_{rs} and ε_{20} are known. Those parameters are calibrated as shown in Table 2. The comparisons between the modified Kent-Park model and experimental results in [2] are shown in Fig. 3. A good agreement was observed, indicating that the modified Kent-Park model could successfully describe the engineering compressive stress-strain relationship of UHPC and UHPFRC.

3. Fracture Evaluation of UHPC/UHPFRC

3.1. Concrete damaged plasticity (CDP) model

The concrete damage plasticity model (CDP) model was employed to simulate the mechanical behavior of UHPC/UHPFRC. The yield function of the CDP model[36] is expressed in Eq.(3). The evolution of the yield surface is controlled by the equivalent plastic strain. The yield surface in-plane stress of the CDP model is shown in Fig. 4.

$$F = \frac{1}{1-\alpha}\left(\bar{q} - 3\alpha\bar{p} + \beta\left\langle\bar{\sigma}_{max}\right\rangle - \gamma\left\langle -\bar{\sigma}_{max}\right\rangle\right) - \bar{\sigma}_c = 0 \tag{3}$$

With:

$$\alpha = \frac{(\sigma_{b0}/\sigma_{c0}) - 1}{2(\sigma_{b0}/\sigma_{c0}) - 1};\ 0 \leqslant \alpha \leqslant 0.5 \tag{4}$$

$$\beta = \frac{\bar{\sigma}_c}{\bar{\sigma}_t}(1-\alpha) - (1+\alpha) \tag{5}$$

$$\gamma = \frac{3(1-K_c)}{2K_c - 1} \tag{6}$$

Where: $\bar{q}$ is the Mises equivalent effective stress; $\bar{p}$ is the hydrostatic pressure stress; $\bar{\sigma}_{max}$is the maximum principal effective stress; σ_{b0}/σ_{c0} is the ratio of initial equi-biaxial compressive yield stress to initial uniaxial compressive yield stress; K_c is the ratio of the second stress invariant on the tensile meridian to that on the compressive meridian at initial yield; $\bar{\sigma}_t$ is the effective tensile cohesion stress; $\bar{\sigma}_c$is the effective compressive cohesion stress.

No associated potential plastic flow is used in the concrete damaged plasticity model. The Drucker-Prager hyperbolic function is used as flow potential G:

$$G = \sqrt{(\varepsilon\sigma_{t0}tan\psi)^2 + \bar{q}^2} - \bar{p}tan\psi \tag{7}$$

Where: ψ is the dilation angle measured in the p-q plane at high confining pressure; σ_{t0} is the uniaxial tensile stress at failure; ε is eccentricity parameter.

Due to lack of sufficient experimental data of UHPC/UHPFRC, the default values of dilation angle ψ (30^0), eccentricity parameter ε(0.1), the ratio of equi-biaxial compressive yield stress to initial uniaxial compressive yield stress σ_{b0}/σ_{c0}(1.16), the second stress invariant on the tensile meridian to that on the compressive meridian at initial yield K_c(0.667) are used.

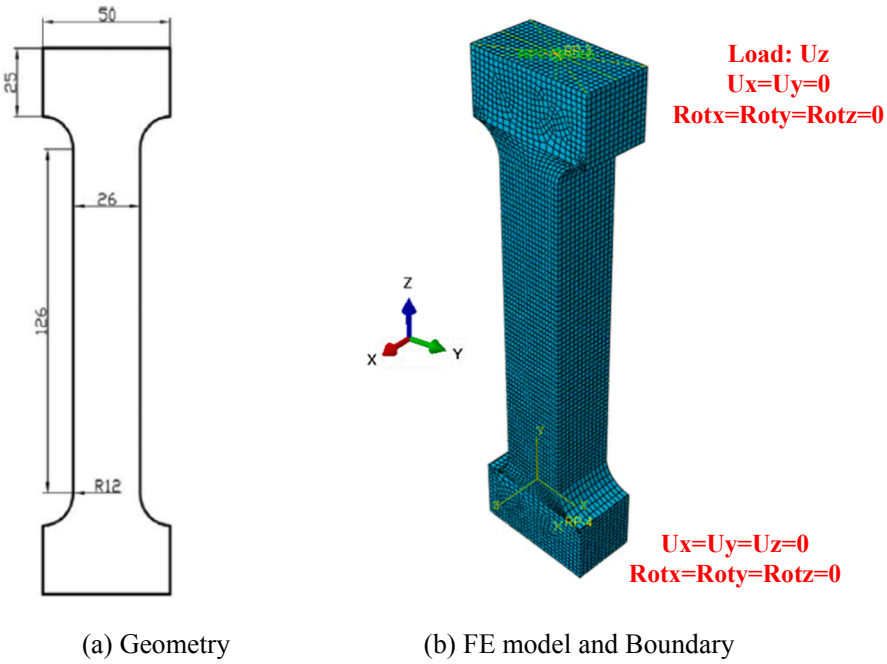

Fig. 5. Geometry and FE model of tensile specimens.

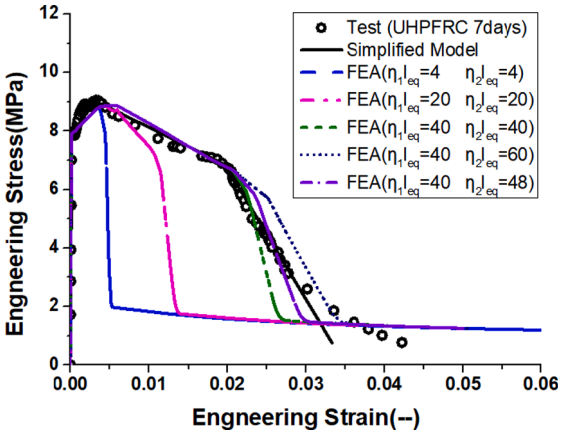

Fig. 6. Schematic of crack displacement calibration.

The UHPC/UHPFRC fails and all stress components are set to zero when either of the following failure criterion is met: (1) the tensile cracking strain $\tilde{\varepsilon}_t^{ck}$ or tensile cracking displacement u_t^{ck} reaches the critical value; $\tilde{\varepsilon}_t^{ck} \geqslant \left(\tilde{\varepsilon}_t^{ck}\right)_f$ or $u_t^{ck} \geqslant \left(u_t^{ck}\right)_f$; (2) the compressive inelastic strain $\tilde{\varepsilon}_c^{in}$ reaches the critical value $\tilde{\varepsilon}_c^{in} \geqslant \left(\tilde{\varepsilon}_c^{in}\right)_f$. The element is deleted from the model when either of the above failure criterion is met.

3.2. Simulation of uniaxial tensile behaviors

The dog-bone tensile specimens were built in the software to simulate the behavior of UHPC and UHPFRC exposed to tensile load. The geometry, FE models and boundary conditions are presented in Fig. 5. Elements C3D8 are used for the tensile model. The bottom surfaces and top surface of tensile specimens are connected to reference point RB and RT using multi-point constraints "MPC", respectively. All degree freedoms of RB are fixed, and all rotation degree freedom and the horizontal displacement UY, UZ, of RT are fixed. The tensile load is applied through a displacement along the vertical direction. ABAQUS/EXPLICIT is used for the calculation with a total step time 1 s and time increment 1×10^{-5} s.

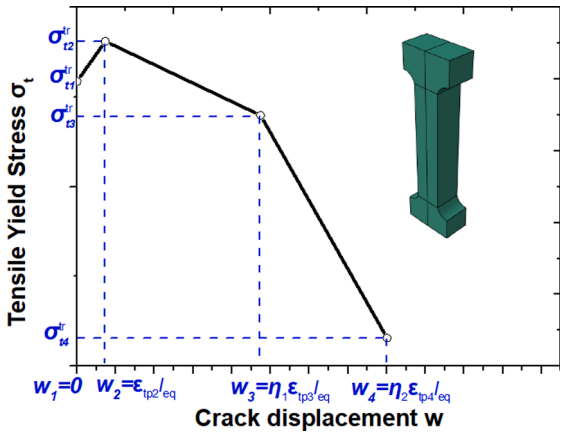

Fig. 7. Simplified tensile yield stress-crack displacement relationship.

Table 3
Parameters of simplified tensile yield stress-crack displacement relationship. (Unit: mm for crack displacement, Mpa for stress).

		w_1	σ_{t1}^{tr}	w_2	σ_{t2}^{tr}	w_3	σ_{t3}^{tr}	w_4	σ_{t4}^{tr}	$\eta_1 l_{eq}$	$\eta_2 l_{eq}$
UHPC	7d	0	3.67	8.7×10^{-5}	4.42	5.3×10^{-3}	3.13	0.0133	0.01	40	48
	14d	0	3.56	1.8×10^{-4}	4.95	7.2×10^{-3}	3.70	0.0166	0.01	40	48
	28d	0	4.76	9.7×10^{-5}	4.76	3.7×10^{-3}	4.09	0.0096	0.01	40	48
UHPCFRC	7d	0	7.93	0.006	9.05	1.046	6.99	2.120	0.79	40	48
	14d	0	7.57	0.004	8.93	1.730	4.22	2.788	0.70	40	48
	28d	0	8.40	0.008	9.17	5.300	7.09	3.197	1.89	40	48

The true tensile stress-strain curve is obtained through Eqs. (8) and (9). To alleviate the mesh size effects, the stress-crack displacement curves were used to describe the uniaxial tensile behaviors. The crack displacement could be simply obtained by the product of plastic strain $\tilde{\varepsilon}_t^p$ and the characteristic element length l_{eq}. However, as shown in Fig. 6, the FE simulation results $FEA\left(\eta_1 l_{eq} = 4\,\eta_2 l_{eq} = 4\right)$ are smaller than the experimental results. This is because microdamage happened after the peak point and Eqs. (8) and (9) could not effectively convert the engineering stress-strain curve to the true stress-strain curve.

$$\varepsilon = ln(1 + \varepsilon_{en}) \tag{8}$$

$$\sigma = \sigma_{en}(1 + \varepsilon_{en}) \tag{9}$$

In order to successfully predict the tensile behaviors after the peak stress, we proposed a simplified tensile yield stress-crack displacement relationship (see Fig. 7) based on the four-linear engineering stress-strain curves proposed in Fig. 1. The true stress, $\sigma_{ti}^{tr}(i = 1 \ldots 4)$, could be easily obtained through engineering stress using Eq. (9). The crack displacement could be obtained by equivalent plastic strain, the characteristic element length l_{eq}, and the empirical revision parameter $\eta_i(i = 1, 2)$. The empirical revision parameters $\eta_i(i = 1, 2)$ could be obtained through the calibration. The calibration process of UHPFRC at 7 days is presented in Fig. 6. The FE prediction agreed best with the experimental results when the $\eta_1 l_{eq} = 40$ and $\eta_2 l_{eq} = 48$. The parameters of the simplified tensile yield stress-crack displacement relationship of UHPC and UHPFRC are calibrated as shown in Table 3. The tensile behavior comparisons between FE prediction and test results are shown in Fig. 8. The good agreement indicates that the proposed simplified tensile yield stress-crack displacement relationship is validated. The fracture displacement w_4 of UHPFRC at 7, 14, and 28 days is 159.4, 168.0, and 333.0 times larger than that of UHPC at 7, 14, and 28 days, respectively.

3.3. Simulation of uniaxial compressive behaviors

The FE analysis was conducted to predict the uniaxial compressive behavior of UHPC and UHPFRC. The FE model and boundary conditions used in the simulation are shown in Fig. 9. The dimension of the load and support plates is 100 mm × 100 mm × 40 mm. The diameter of the cylinder specimen is 26 mm, and the length of the cylinder specimen is 50 mm. All degree freedoms of the bottom surfaces of the support plate are fixed. The top surface of the load plate is connected to a reference point RP through multi-point constraints "MPC". The tensile load is applied through the reference point RP with a displacement along the vertical direction. ABAQUS/EXPLICIT is used for the calculation with a total step time 1 s and time increment 1×10^{-5}s. Element type C3D8 was used for the compressive model. Surface to surface contact is built between cylinder specimen and support/load specimen, with a "hard" property for normal direction and 0.1 friction coefficient for tangential direction.

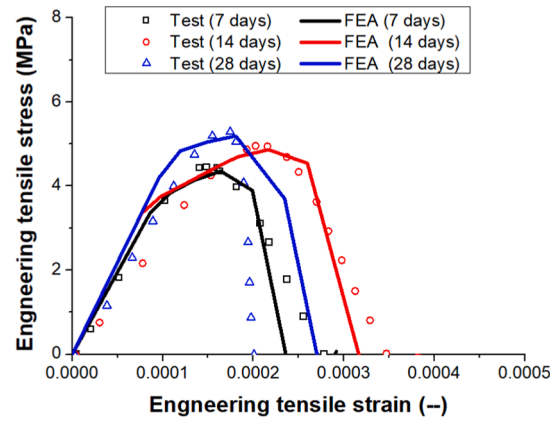

(a)UHPC

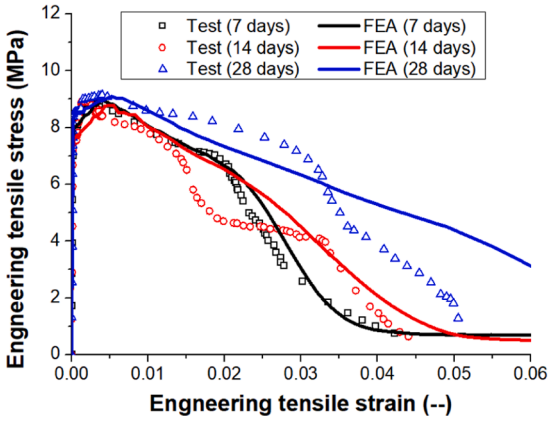

(b) UHPCFRC

Fig. 8. Comparison tensile behavior between experimental and numerical results.

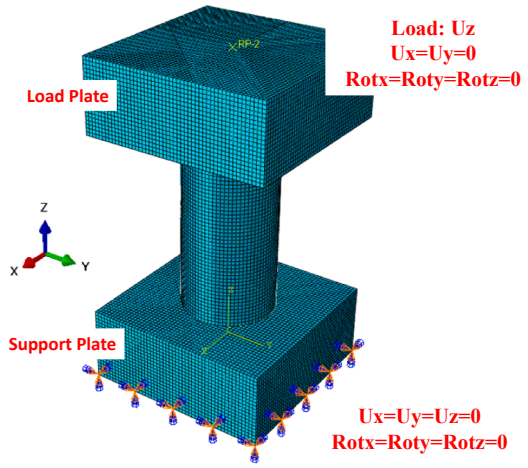

Fig. 9. FE of Compressive specimens.

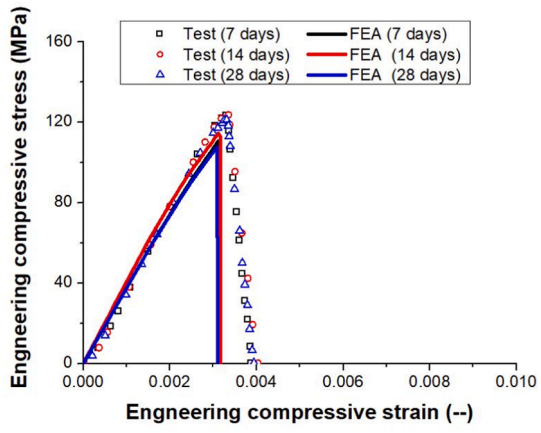

(a) UHPC

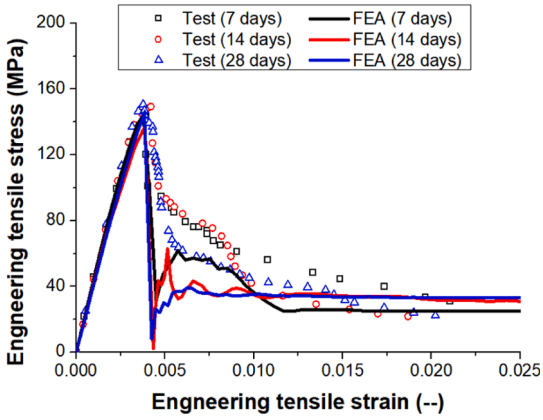

(b) UHPCFRC

Fig. 10. Comparison between experimental and numerical results.

Table 4
Fracture parameters of UHPC and UHPFRC.

		Tensile crack displacement (mm)	Compressive equivalent inelastic strain
UHPC	7d	0.0133	0.004
	14d	0.0166	0.005
	28d	0.0096	0.004
UHPCFRC	7d	2.120	0.020
	14d	2.788	0.020
	28d	3.197	0.020

The uniaxial compressive true stress-strain relationship was directly used in the FE simulation based on the engineering compressive stress-strain relationship presented in Section 2.2. The comparisons between FE prediction and experimental results are shown in Fig. 10. A good agreement was observed, except that the fracture engineering strain of UHPC is relatively smaller than the experimental results.

3.4. Fracture parameters

The elements will be deleted from the model when $u_t^{ck} \geqslant \left(u_t^{ck}\right)_f$ or $\tilde{\varepsilon}_c^{in} \geqslant \left(\tilde{\varepsilon}_c^{in}\right)_f$. The critical tensile cracking displacement $\left(u_t^{ck}\right)_f$ is proposed to be identical w_4 in Fig. 7, and $\left(\tilde{\varepsilon}_c^{in}\right)_f$ is proposed to be identical to the plastic strain corresponding to the engineering strain

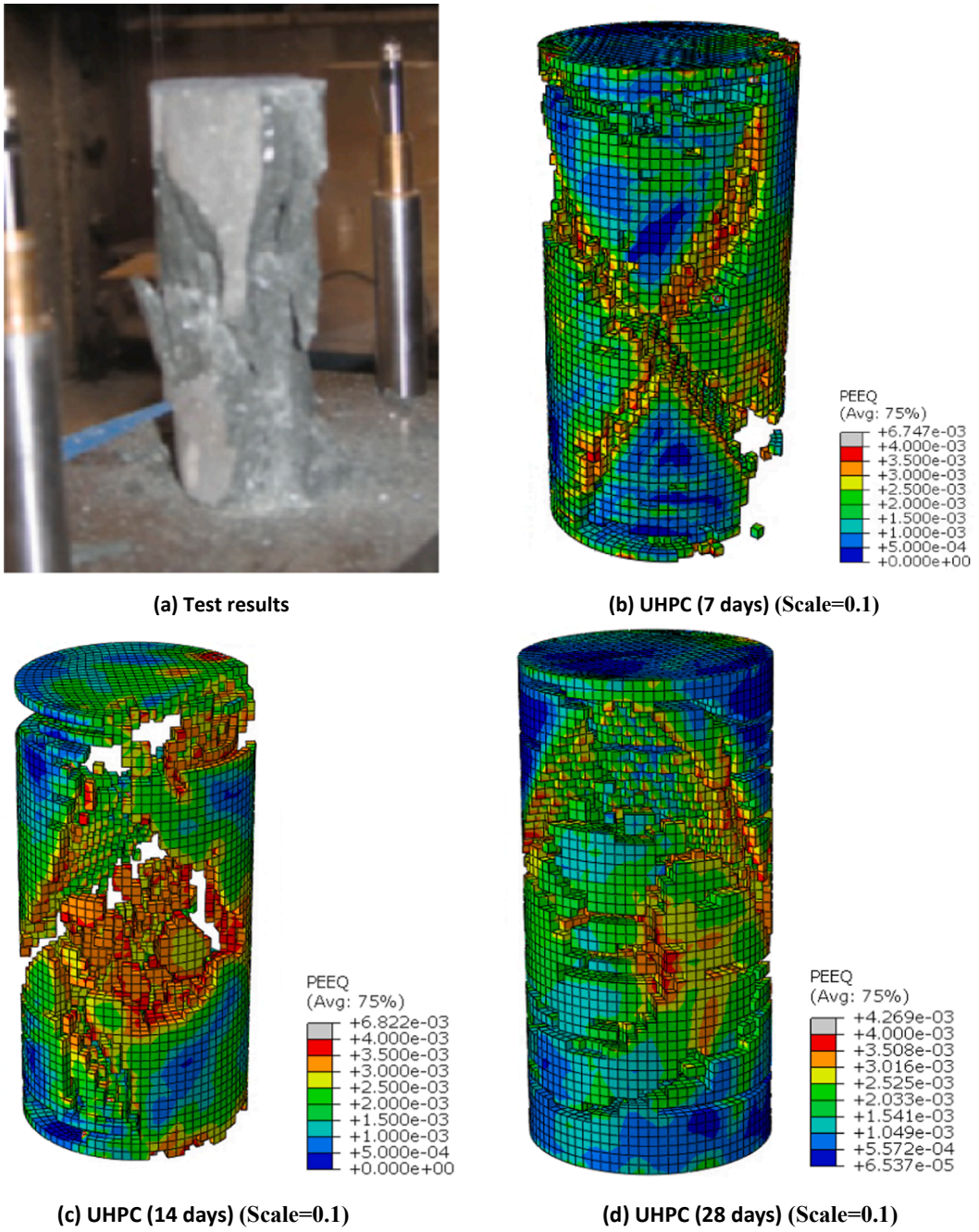

(a) Test results

(b) UHPC (7 days) (Scale=0.1)

(c) UHPC (14 days) (Scale=0.1)

(d) UHPC (28 days) (Scale=0.1)

Fig. 11. Failure model comparison of compressive specimens of UHPC. (Failure photo is from[2]).

ε_{20} in Eq.(2). The fracture parameters of UHPC and UHPFRC at 7, 14, and 28 days are summarized in Table 4.

The crack pattern comparisons between FE prediction and test results are shown in Figs. 11 and 12 for UHPC, and Figs. 13 and 14 for UHPFRC. The predicted failure mode of UHPC and UHPFRC specimens generally agreed well with the test results. As shown in Figs. 11 and 13, the failure mode of UHPC exposed to uniaxial compressive from both tests and FE simulation presented an explosive pattern; in contrast, the failure mode of UHPFRC exposed to uniaxial compressive from both tests and FE simulation presented a major incline crack. As shown in Figs. 12 and 14, the tensile failure modes of UHPC and UHPFRC are quite similar, which present a horizontal crack pattern. Noted that the failure position in FE simulation is different from that in the experiment, which is suggested to be improved in the future.

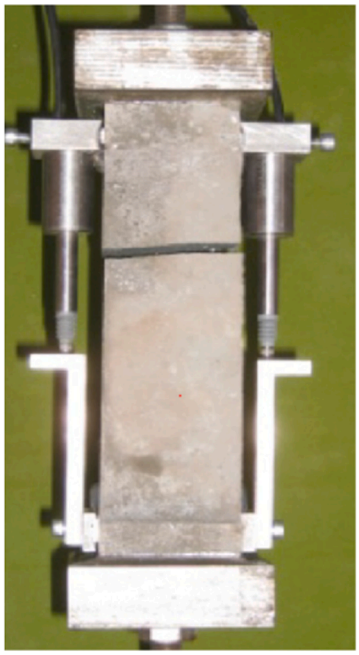

(a) Test results

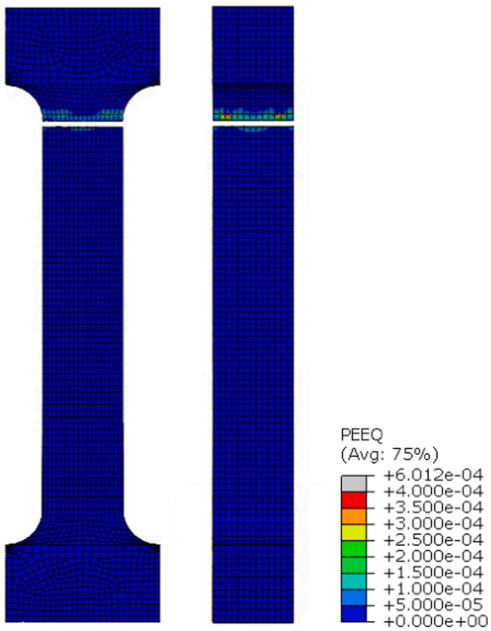

(b) UHPC (7 days) (Scale=1)

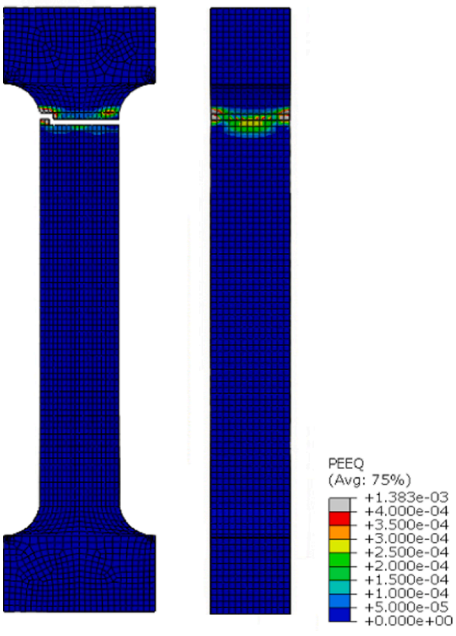

(c) UHPC (14 days) (Scale=1)

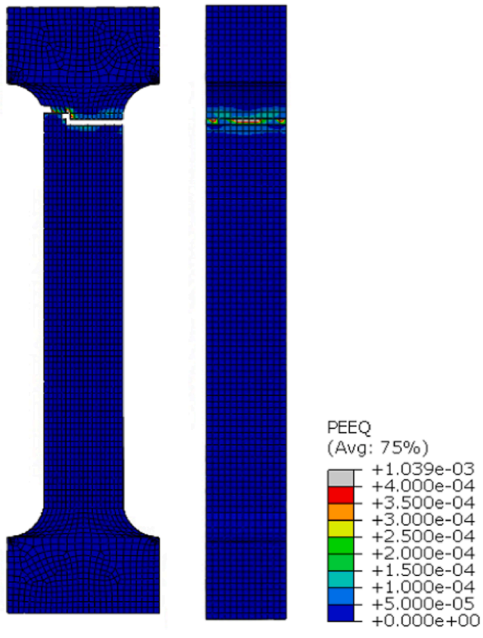

(d) UHPC (28 days) (Scale=1)

Fig. 12. Failure model comparison of tensile specimens of UHPC. (Failure photo is from[2]).

(a) Failure mode of UHPCFRC

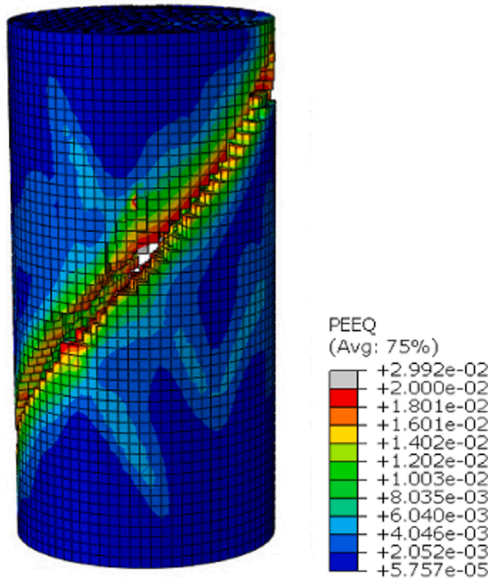

(b) UHPCFRC at 7 day (Scale=0.1)

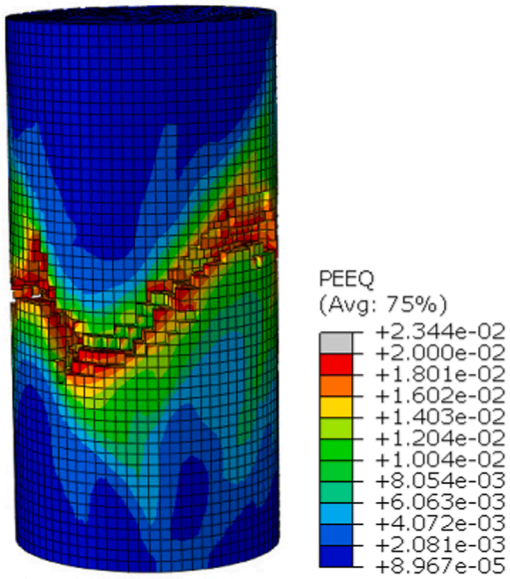

(c) UHPCFRC at 14 day (Scale=0.1)

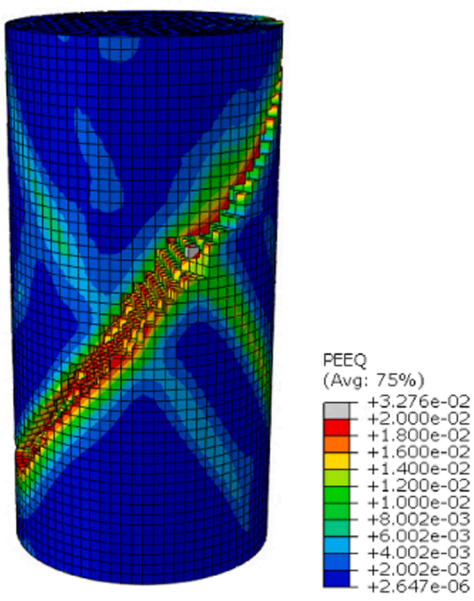

(d) UHPCFRC at 28 day (Scale=0.1)

Fig. 13. Compressive failure modes of UHPCFRC specimens (Failure photo is from[2]).

4. Mixed Mode Crack Propagations

For a better understanding of the behavior of UHPC and UHPFRC exposed to biaxial loading, numerical simulation on the double-notched specimens exposed to combined shear-tensile and shear-compressive forces was carried out using validated material model presented in Section 3. As shown in Fig. 15-a, the geometry of the double-notched specimen is 200 mm × 200 mm × 50 mm; the length and height of pre-notched crack are 20 mm and 10 mm, respectively. As shown in Fig. 15(b), two types of loading were applied, namely shear-tensile and shear-compressive loadings. All degree freedoms of the bottom surface of double-notched specimens were fixed, and the horizontal displacement UZ at the top surface was also fixed. The proportional displacement UX and UY were applied to the top

(a) Test results

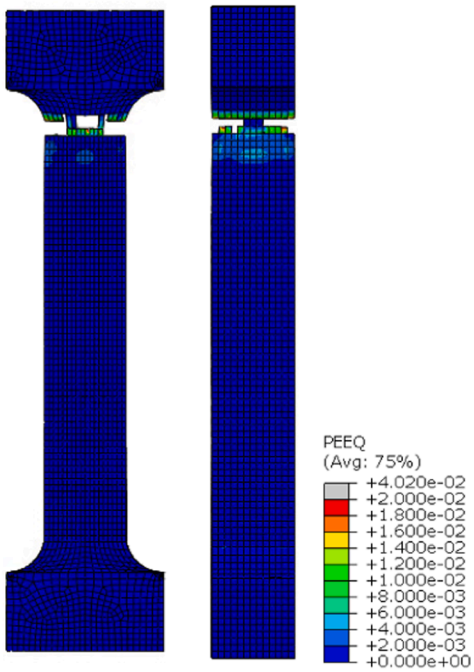

(b) UHPCFRC at 7 day (Scale=1.0)

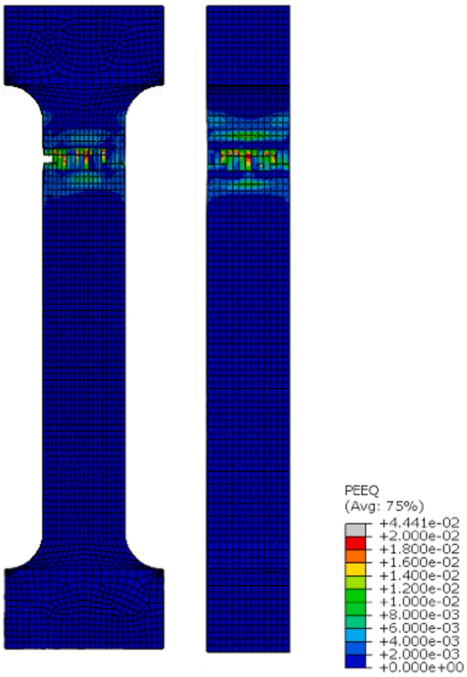

(c) UHPCFRC at 14 day (Scale=1.0)

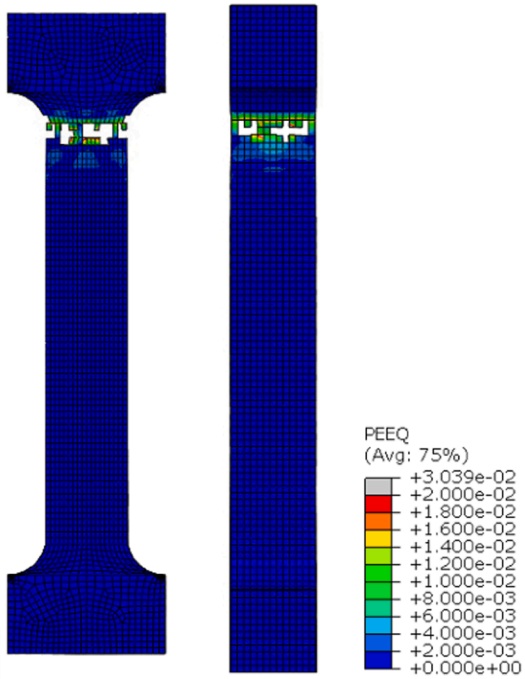

(d) UHPCFRC at 28 day (Scale=1.0)

Fig. 14. Failure mode comparisons of Tensile UHPCFRC specimens (Failure photo is from[2]).

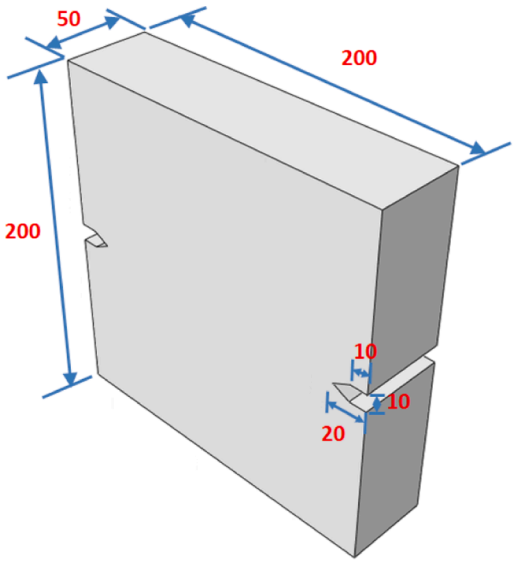

(a) Geometry of mixed mode crack propagation

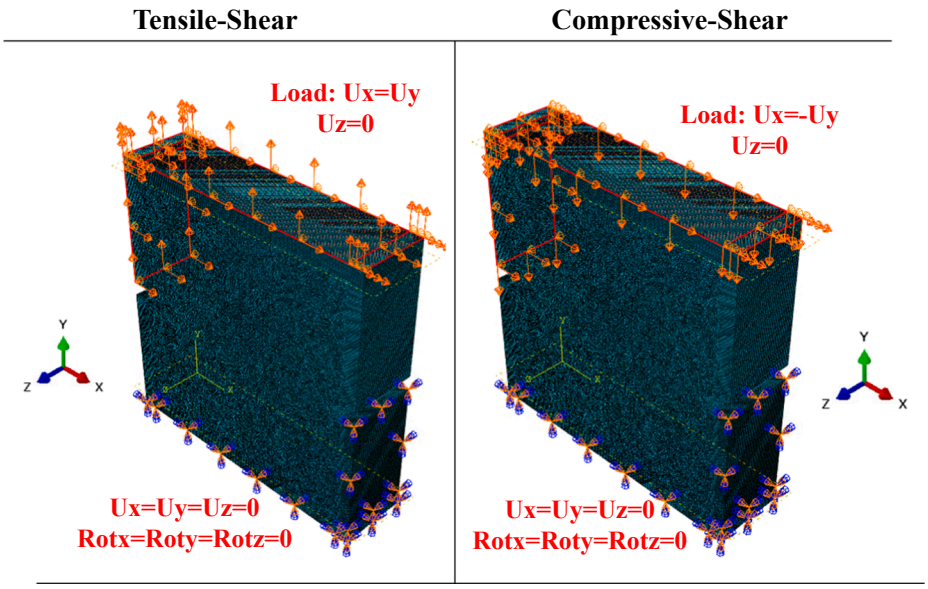

(b) Mesh and Boundary conditions

Fig. 15. Mixed mode crack propagation specimens.

surface of double-notched specimens to generate the combined shear-tensile and shear-compressive loading status. ABAQUS/EXPLICIT was used for the calculation with a total step time 1 s and time increment 1×10^{-5} s. Element type C3D8 was used for the mixed crack propagation model.

The load–displacement curves of double notched specimens made of UHPC and UHPFRC exposed to the combined tensile-shear loading are shown in Fig. 16. The double notched specimens made of UHPC is relatively brittle, and the specimens fail when the displacement reaches approximately 0.5 mm. The force F_x of UHPC specimen reaches the peak when the displacement is 0.19 mm while the force F_y of UHPC specimen reaches to the peak when the displacement is 0.02 mm. Both the forces F_x and F_y of UHPC specimen drop quickly after reaching the peak point. The double notched specimens made of UHPFRC is more ductile, the failure displacement is 1.8 mm. Both the forces F_x and F_y of UHPFRC specimen reach the peak when the displacement is around 0.05 mm and gradually decreases after the peak point.

Fig. 17 and Fig. 18 present the crack propagation process of UHPC and UHPFRC specimens exposed to combined tensile-shear

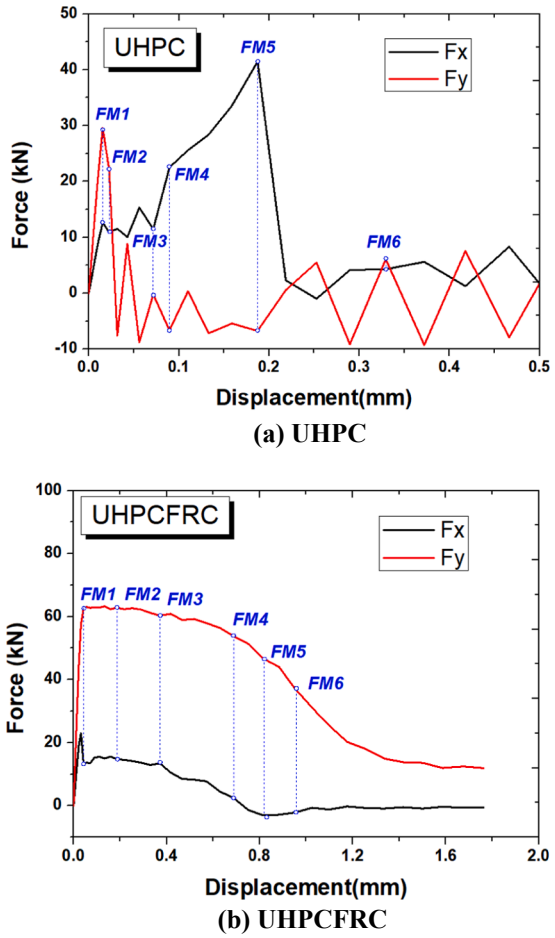

Fig. 16. Load-displacement relationship under combined tensile and shear loading.

loading. The crack presents a curved path for the UHPC double notched specimens, and an almost straight line pattern for the UHPFRC double notched specimens.

The load–displacement curves of double notched specimens made of UHPC and UHPFRC exposed to the combined compressive-shear loading are shown in Fig. 19. Both the forces F_x and F_y of UHPC specimen reach the peak when the displacement increases to 0.09 mm and drop to almost zero when the displacement increases to around 0.16 mm. The force F_x of UHPFRC specimen reaches the peak when the displacement is 0.25 mm while the force F_y of UHPC specimen reaches the peak when the displacement is 0.22 mm. Both the forces F_x and F_y of UHPFRC specimen drop to almost zero when the displacement increases to around 0.42 mm.

The failure displacement of double notched specimens made of UHPC and UHPFRC exposed to the combined compressive-shear loading is smaller than that exposed to the combined tensile-shear loading. The maximum forces F_x and F_y of double notched specimens made of UHPC and UHPFRC exposed to the combined compressive-shear loading is larger than that exposed to the combined tensile-shear loading.

Fig. 20 and Fig. 21 show the crack propagation process of UHPC and UHPFRC specimens exposed to combined compressive-shear loading. The crack of UHPC and UHPFRC double notched specimens both presented a curved path. The crack of UHPC and UHPFRC specimens initiated near the notch and final failure happened when the crack from two notches coalesced together by an incline major crack. Several crack branches were observed for the UHPC double notched specimens during crack propagation. The UHPFRC specimens only form one major crack during combined compressive-shear loading.

5. Conclusions

The development of numerical simulation is fundamental for the design and construction of structures made of ultra-high-performance concrete (UHPC) and ultra-high-performance fiber-reinforced concrete (UHPFRC). An attempt was made to simulate the fracture of UHPC and UHPFRC using the CDP model and element deletion strategies in this paper. For a better understanding of the behavior of UHPC and UHPFRC exposed to biaxial loading, numerical simulation on the double-notched specimens exposed to the combined shear-tensile and the shear-compressive forces was carried out using a validated material model. Following conclusions are

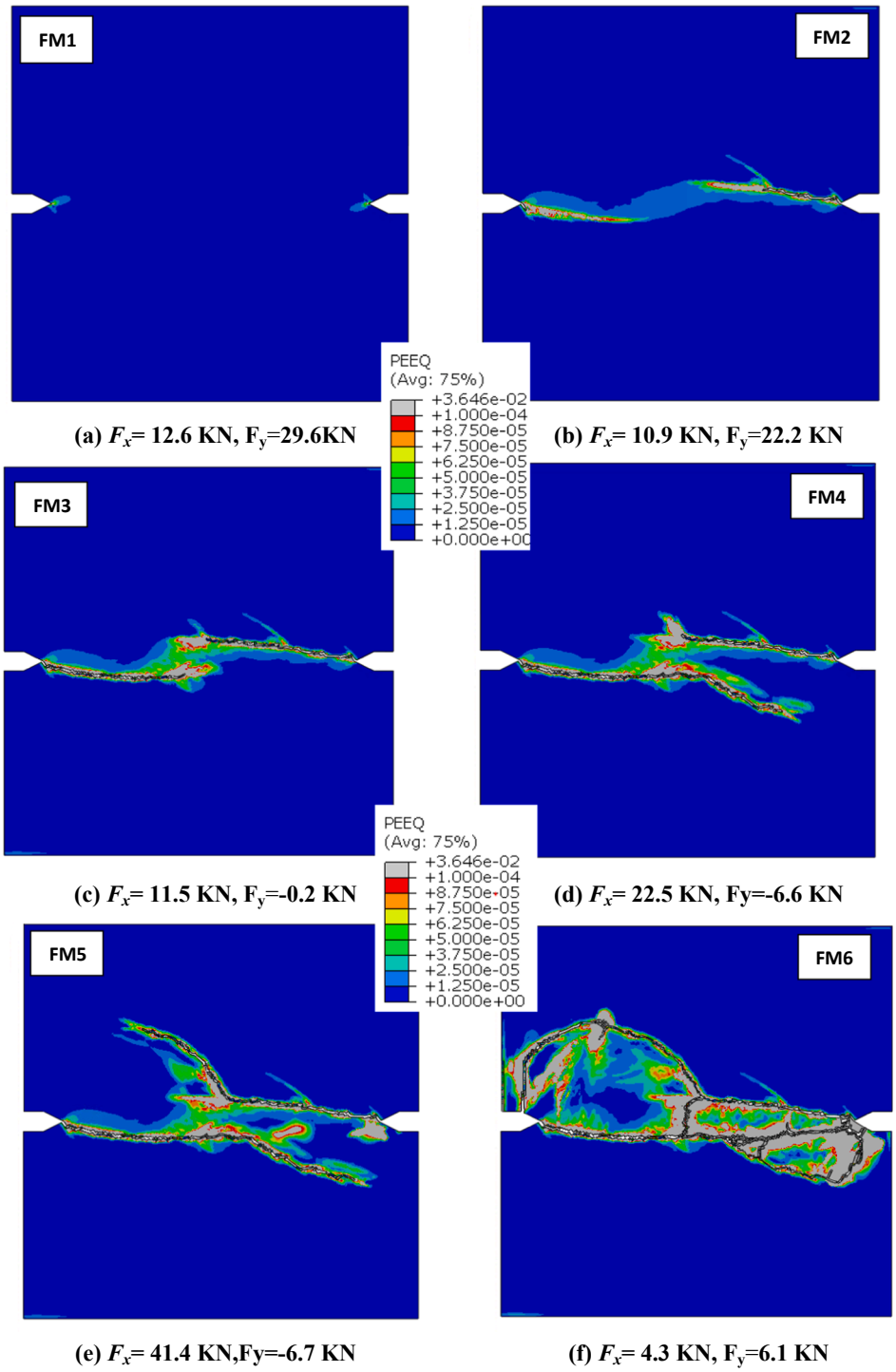

Fig. 17. Crack propagation of UHPC (28 days) under tensile and shear loading.

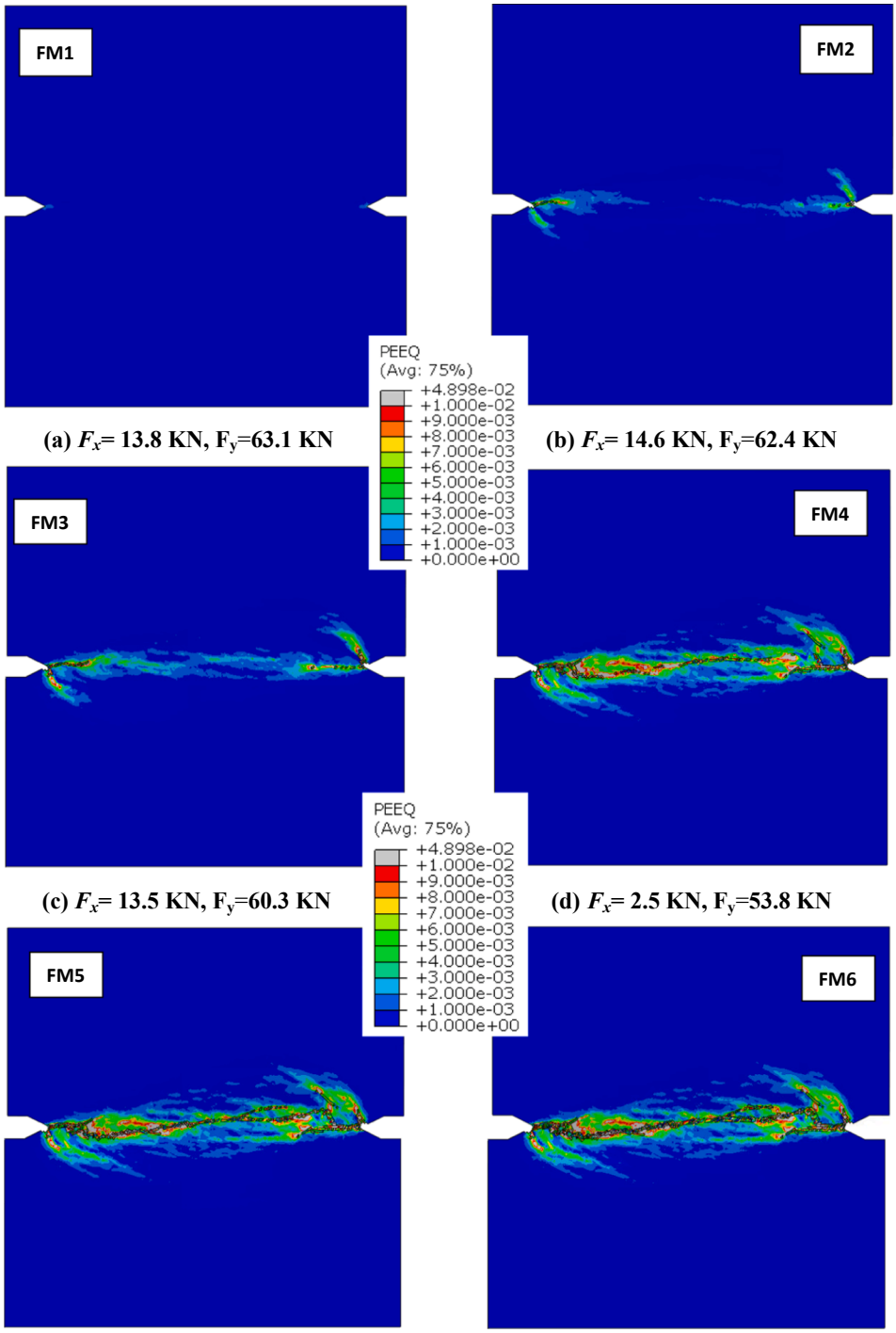

Fig. 18. Crack propagation of UHPCFRC (28 days) under tensile and shear loading.

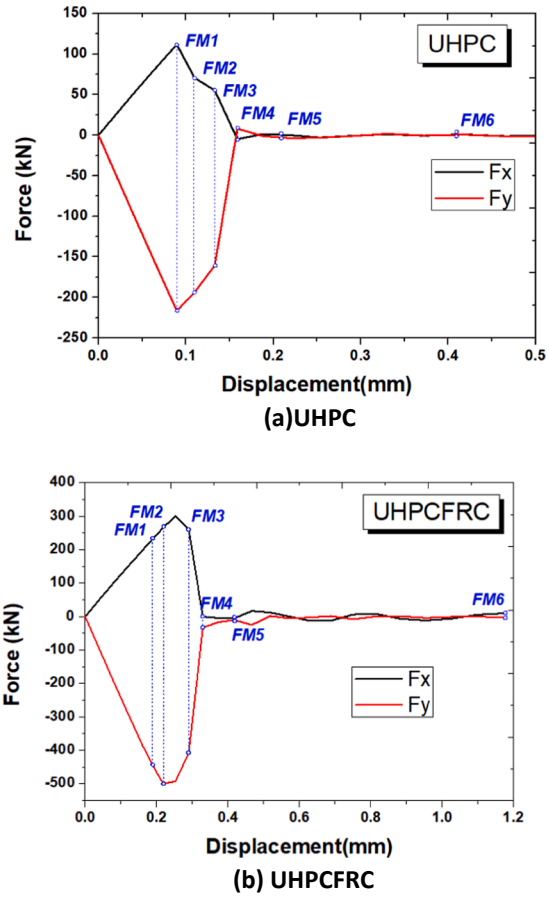

Fig. 19. Load-displacement relationship under combined compressive and shear loading.

drawn:

(1) Four-linear curves and the modified Kent–Park model were proposed to describe the engineering tensile and compressive stress-strain relationships, respectively. A good agreement was observed between the simplified model and test results regarding the engineering stress-strain relationship.
(2) The tensile and compressive behaviors of UHPC and UHPFRC were predicted using the CDP model. The method to obtain the input values, including the tensile-crack displacement relationship, compressive stress-strain relationship, and fracture parameters was suggested. The simulation results were successfully validated by the test results in the literature.
(3) The failure displacement of double notched specimens made of UHPC and UHPFRC exposed to the combined compressive-shear loading is smaller than that exposed to the combined tensile and shear loading. The maximum force of double notched specimens made of UHPC and UHPFRC exposed to the combined compressive-shear loading is larger than that exposed to the combined tensile-shear loading.
(4) The crack presented a curved path for the UHPC double notched specimens but presented an almost straight line pattern for the UHPFRC double notched specimens when exposed to tensile-shear loading. The crack of UHPC and UHPFRC double notched specimens presented a curved path, and several crack branches were observed for the UHPC specimens but the UHPFRC specimens only form one major crack when exposed to combined compressive-shear loading.

Declaration of Competing Interest

The authors declare that they have no known competing financial interests or personal relationships that could have appeared to influence the work reported in this paper.

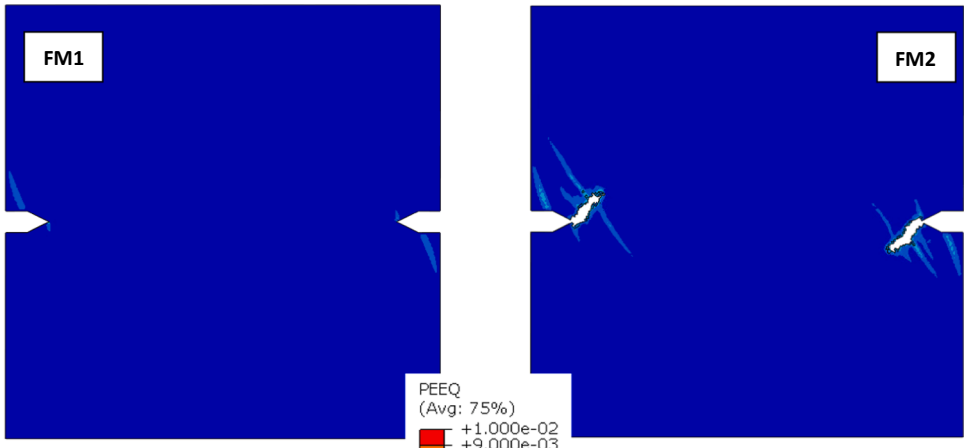

(a) F_x= 111.7 KN, F_y=-216.5 KN (b) F_x= 70.5 KN, F_y=-193.6 KN

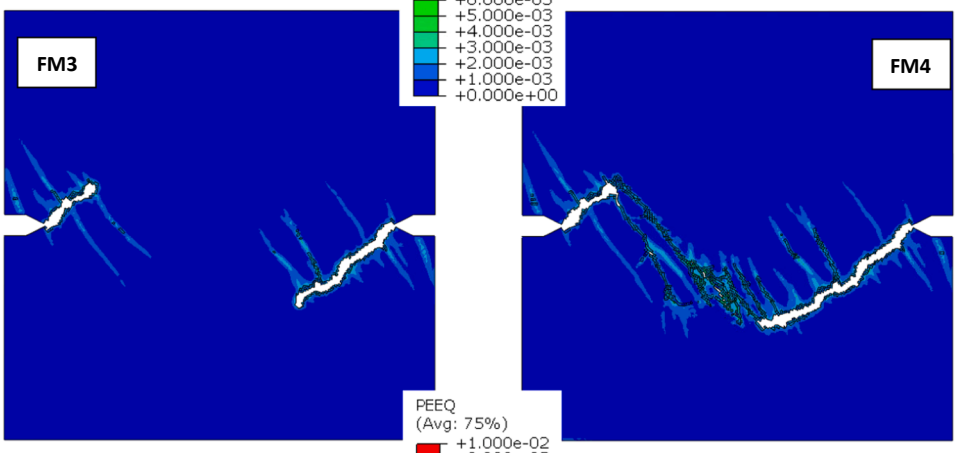

(c) F_x= 55.2 KN, F_y=-160.5 KN (d) F_x= -4.8 KN, F_y=8.0 KN

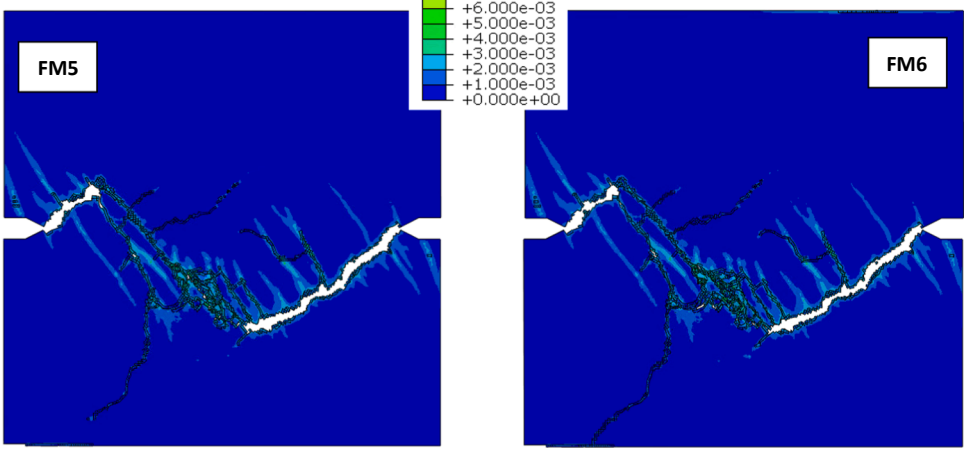

(e) F_x= -1.2 KN, F_y=-1.0KN (f) F_x= -0.9 KN, F_y=0.7 KN

Fig. 20. Crack propagation of UHPC (28 days) under compressive and shear loading.

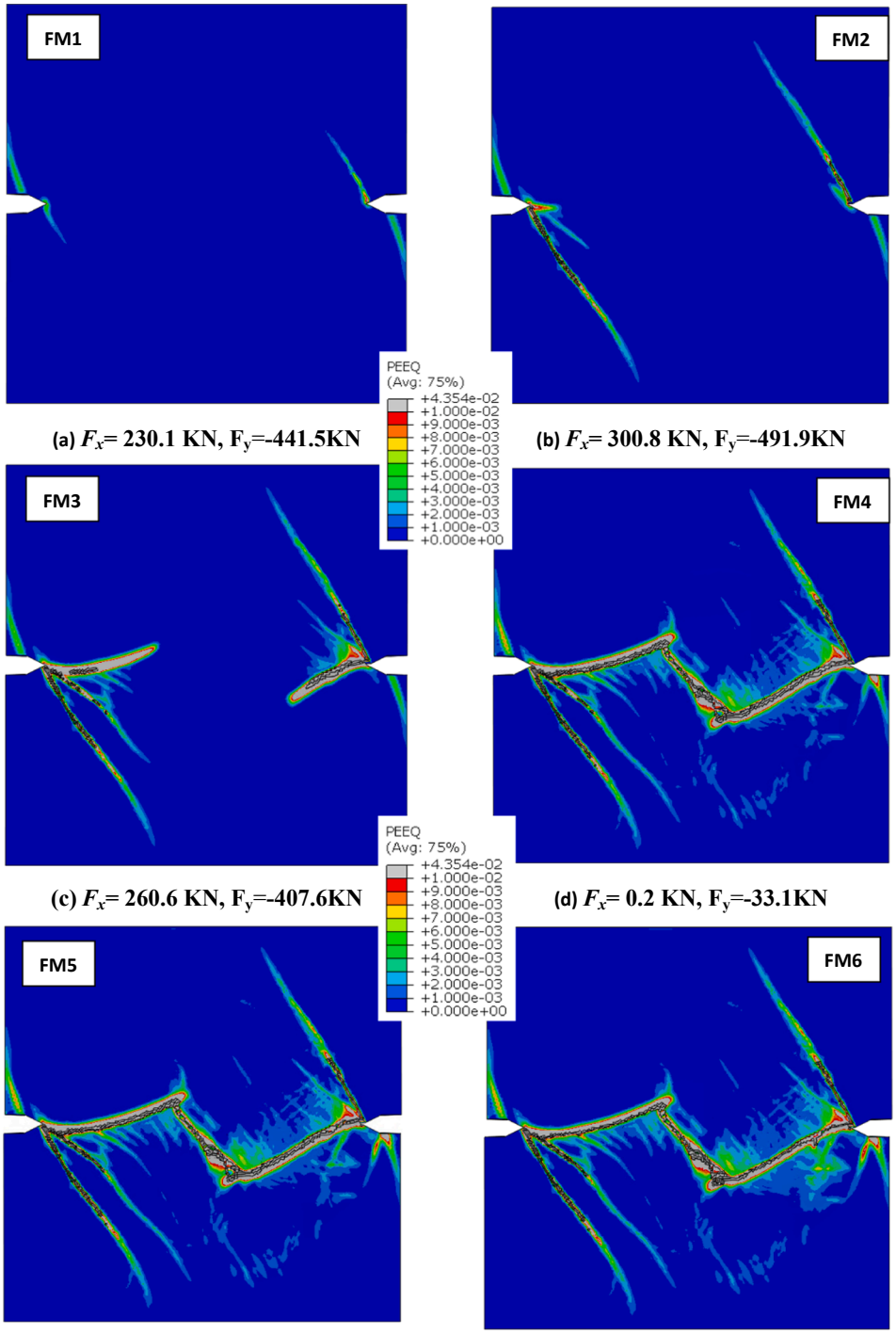

Fig. 21. Crack propagation of UHPCFRC (28 days) under compressive and shear loading.

Acknowledgements

The authors gratefully acknowledge the financial support provided by the National Natural Science Foundation (Grants #51808398 & 52078362) of the People's Republic of China. The author José A.F.O. Correia would like to acknowledge the support given by base funding - UIDB/04708/2020 and programmatic funding - UIDP/04708/2020 of the CONSTRUCT - Instituto de I&D em Estruturas e Construções - funded by national funds through the FCT/MCTES (PIDDAC).

References

[1] K. Habel, M. Viviani, E. Denarié, E. Brühwiler, Development of the mechanical properties of an ultra-high performance fiber reinforced concrete (UHPFRC), Cem. Concr. Res. 36 (2006) 1362–1370.
[2] A.M.T. Hassan, S.W. Jones, G.H. Mahmud, Experimental test methods to determine the uniaxial tensile and compressive behaviour of ultra high performance fibre reinforced concrete (UHPFRC), Constr. Build. Mater. 37 (2012) 874–882.
[3] M.M. Reda, N.G. Shrive, J.E. Gillott, Microstructural investigation of innovative UHPC, Cem. Concr. Res. 29 (1999) 323–329.
[4] P. Richard, M. Cheyrezy, Composition of reactive powder concretes, Cem. Concr. Res. 25 (1995) 1501–1511.
[5] B.H. Oh, Flexural analysis of reinforced concrete beams containing steel fibers, J. Struct. Eng. 118 (1992) 2821–2835.
[6] S.A. Ashour, F.F. Wafa, Flexural behavior of high-strength fiber reinforced concrete beams, Struct. J. 90 (1993) 279–287.
[7] G. Campione, M.L. Mangiavillano, Fibrous reinforced concrete beams in flexure: Experimental investigation, analytical modelling and design considerations, Eng. Struct. 30 (2008) 2970–2980.
[8] M.A. Saleem, A. Mirmiran, J. Xia, K. Mackie, Ultra-High-Performance Concrete Bridge Deck Reinforced with High-Strength Steel, ACI Struct. J. 108 (2011).
[9] B.A. Graybeal, Flexural behavior of an ultrahigh-performance concrete I-girder, J. Bridg. Eng. 13 (2008) 602–610.
[10] Z. Wang, J. Wang, T. Liu, F. Zhang, Modeling seismic performance of high-strength steel–ultra-high-performance concrete piers with modified Kent-Park model using fiber elements, Adv. Mech. Eng. 8 (2016), 1687814016633411.
[11] H.G. Russell, B.A. Graybeal, H.G. Russell, Ultra-high performance concrete: A state-of-the-art report for the bridge community. United States. Federal Highway Administration. Office of Infrastructure…; (2013).
[12] S.V. Shann, Application of ultra high performance concrete (UHPC) as a thin-bonded overlay for concrete bridge decks (2012).
[13] M. Bagheri, S.A. Hosseini, B. Keshtegar, J.A.F.O. Correia, N.-T. Trung, Uncertain time-dependent reliability analysis of corroded RC structures applying three-term conjugate method, Eng. Fail. Anal. (2020).
[14] P. Stroński, W. Błażejewski, T. Socha, A. Denisiewicz, K. Kula, G. Lesiuk, et al., Influence of reinforcement Type on Flexural Behaviour of Reinforced Concrete Beams, Proc. Inst. Civ. Eng. Eng. (2020) 1–9.
[15] M. Smolnicki, M. Cieciura, G. Lesiuk, J. Correia, P. Stabla, Fracture behaviour of engineering stone material, Int. J. Struct. Integr. (2019).
[16] S.S.R. Pereira, H. Carvalho, J.V.F. Dias, V.R.V. Mendes, P.A. Montenegro, Behavior of precast reinforced concrete columns subjected to monotonic short-term loading, Frat. Ed. Integrita Strutt. 13 (2019) 242–250.
[17] C.C. Silva, R.B. Caldas, R.H. Fakury, H. Carvalho, J.V.F. Dias, Web Rotational Stiffness of Continuous Steel-Concrete Composite Castellated Beams, Frat Ed Integrità Strutt 13 (2019) 264–275.
[18] J. He, S. Wang, Y. Liu, D. Wang, H. Xin, Shear behavior of steel I-girder with stiffened corrugated web, Part II: Numerical study, Thin-Walled Struct. (2020) 147.
[19] Y. Zhang, Y. Liu, H. Xin, J. He, Numerical parametric study on ultimate load and ductility of concrete encased equal-leg angle steel composite columns, Eng. Struct. 200 (2019) 109679.
[20] Y. Liu, H. Xin, J. He, D. Xue, B. Ma, Experimental and analytical study on fatigue behavior of composite truss joints, Jcsr 83 (2013) 21–36, https://doi.org/10.1016/j.jcsr.2012.12.020.
[21] H. Xin, Y. Liu, J. He, Y. Zhang, Experimental and analytical study on stiffened steel segment of hybrid structure, J. Constr. Steel Res. 100 (2014) 237–258.
[22] Y. Liu, H. Xin, Y. Liu, Load transfer mechanism and fatigue performance evaluation of suspender-girder composite anchorage joints at serviceability stage, J. Constr. Steel Res. 145 (2018) 82–96.
[23] Y. Liu, S. Wang, H. Xin, Y. Liu, Evaluation on out-of-plane shear stiffness and ultimate capacity of perfobond connector, J. Constr. Steel Res. 105850 (2019).
[24] Y. Liu, H. Xin, Y. Liu, Experimental and analytical study on shear mechanism of rubber-ring perfobond connector, Eng. Struct. 197 (2019) 109382.
[25] Z. Xiong, Y. Liu, Y. Zuo, H. Xin, Experimental evaluation of shear behavior of pultruded GFRP perforated connectors embedded in concrete, Compos. Struct. 222 (2019) 110938.
[26] Y. Zuo, A. Mosallam, H. Xin, Y. Liu, J. He, Flexural performance of a hybrid GFRP-concrete bridge deck with composite T-shaped perforated rib connectors, Compos. Struct. 194 (2018) 263–278.
[27] H. Xin, Y. Liu, A. Du, Thermal analysis on composite girder with hybrid GFRP-concrete deck (2015) 5.
[28] H. Xin Y. Liu J. He H. Fan Y. Zhang, Fatigue behavior of hybrid GFRP-concrete bridge decks under sagging moment, 4 (2015) 925–946.
[29] T. Soetens, S. Matthys, Different methods to model the post-cracking behaviour of hooked-end steel fibre reinforced concrete, Constr. Build. Mater. 73 (2014) 458–471.
[30] J.Á. López, P. Serna, J. Navarro-Gregori, E. Camacho, An inverse analysis method based on deflection to curvature transformation to determine the tensile properties of UHPFRC, Mater. Struct. 48 (2015) 3703–3718.
[31] J.D. Ríos, C. Leiva, M.P. Ariza, S. Seitl, H. Cifuentes, Analysis of the tensile fracture properties of ultra-high-strength fiber-reinforced concrete with different types of steel fibers by X-ray tomography, Mater. Des. 165 (2019) 107582.
[32] J. Li, C. Wu, H. Hao, An experimental and numerical study of reinforced ultra-high performance concrete slabs under blast loads, Mater. Des. 82 (2015) 64–76.
[33] S.-P. Zhu, B. Keshtegar, S. Chakraborty, N.-T. Trung, Novel probabilistic model for searching most probable point in structural reliability analysis, Comput. Methods Appl. Mech. Eng. 366 (2020) 113027.
[34] Y. Ai, S.-P. Zhu, D. Liao, J.A.F.O. Correia, A.M.P. De Jesus, B. Keshtegar, Probabilistic modelling of notch fatigue and size effect of components using highly stressed volume approach, Int. J. Fatigue 127 (2019) 110–119.
[35] B. Keshtegar, O. Kisi, RM5Tree: Radial basis M5 model tree for accurate structural reliability analysis, Reliab. Eng. Syst. Saf. 180 (2018) 49–61.
[36] V. Abaqus, Documentation, Dassault Syst Simulia Corp 2019 (2019) 651.
[37] D.C. Kent, R. Park, Flexural members with confined concrete, J. Struct. Div. (1971).
[38] B.D. Scott, R. Park, M.J.N. Priestley, Stress-strain behavior of concrete confined by overlapping hoops at low and high strain rates, J. Proc. 79 (1982) 13–27.